Journal of Sol-Gel Science and Technology (2022) 104:566–579
https://doi.org/10.1007/s10971-022-05800-5

INVITED PAPER: NANO-STRUCTURED MATERIALS (PARTICLES, FIBERS, COLLOIDS, COMPOSITES, ETC.)

Microporous structure control of SiO_2-ZrO_2 composite membranes via Yttrium doping and an evaluation of thermal stability

Sulaiman Oladipo Lawal[1] · Yuya Takahashi[1] · Hiroki Nagasawa[1] · Toshinori Tsuru[1] · Masakoto Kanezashi[1]

Received: 1 February 2022 / Accepted: 1 April 2022 / Published online: 23 April 2022

Abstract

Long-term thermal stability is one of the biggest challenges in the utilization of inorganic ceramic membranes in high-temperature separation and membrane reactor applications. This work demonstrated that yttrium doping into SiO_2-ZrO_2 enabled a membrane to maintain stable N_2 permeance in a long-term permeation test at 850 °C. Characterization techniques such as DLS, FTIR, XRD, and N_2 adsorption confirmed that doping with an yttrium/zirconium molar ratio of 1/9 was optimal. A comparison of the thermal stabilities of pristine SiO_2-ZrO_2 and Y-doped SiO_2-ZrO_2 samples calcined at 550–850 °C via XRD and N_2 adsorptions revealed that doping with yttria significantly minimized phase segregation and microstructural densification. Furthermore, a membrane prepared at 550 °C from pristine SiO_2-ZrO_2 showed an immediate decline in N_2 permeance from 6.0×10^{-6} to 0.75×10^{-6} mol m^{-2} s^{-1} Pa^{-1} during a 20-hour, long-term, thermal-stability test conducted at 850 °C. By contrast, after 24 h at 850 °C a Y-SiO_2-ZrO_2-derived membrane showed a reduction of only 5.5×10^{-6} to 5.0×10^{-6} mol m^{-2} s^{-1} Pa^{-1}. Thus, the improved thermal stability of this SiO_2-ZrO_2 composite via yttrium doping heralds the opportunity for ceramic membranes that are more robust.

Graphical Abstract

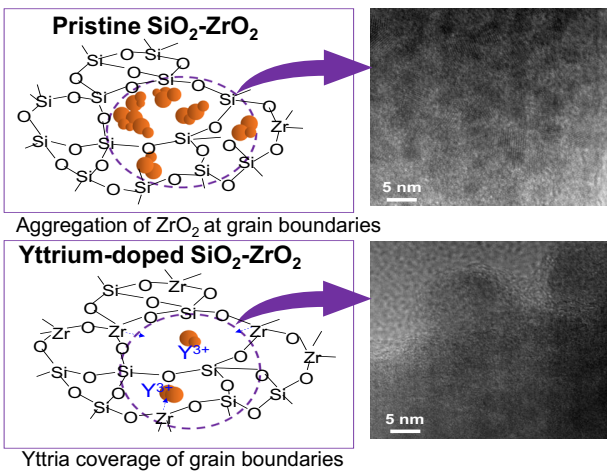

Keywords Silica-zirconia · Yttrium doping · Thermal stability · Membrane support · Gas separation membrane

Supplementary information The online version contains supplementary material available at https://doi.org/10.1007/s10971-022-05800-5.

✉ Masakoto Kanezashi
kanezashi@hiroshima-u.ac.jp

[1] Chemical Engineering Program, Graduate School of Advanced Science and Engineering, Hiroshima University, 1-4-1 Kagamiyama, Higashi-Hiroshima 739-8527, Japan

Highlights

- Yttrium was successfully doped into SiO_2-ZrO_2 via a sol-gel process
- The optimal doping molar ratio of Y/Zr was 1/9
- Yttrium-doped SiO_2-ZrO_2 displayed better thermal stability than pristine SiO_2-ZrO_2
- Membranes derived from yttrium-doped SiO_2-ZrO_2 maintained a stable long-term permeance at 850 °C

1 Introduction

Over the past five decades, arguably the most important development in membrane technology has been the improvement of permselectivity, thermal and hydrothermal robustness, and chemical stability via the incorporation of metal oxides into membrane morphologies [1, 2]. The roles of metal oxides in membrane technology take several forms. For example, silica, arguably the most popular, has been extensively studied and found to possess particularly sharp molecular sieving ability because of the nature of the amorphous phase. Membranes fabricated from titania and zirconia have been applied to nanofiltration because of their chemical and thermal stability. Compositing SiO_2 with alumina and zirconia has also proven very beneficial in several applications. SiO_2-Al_2O_3, and SiO_2-ZrO_2 have been applied to gas separation, pervaporation, and nanofiltration with favorable results [3–7]. Furthermore, metal oxide particles can serve as filler agents to control the polymer microstructure such as in mixed-matrix membranes [8, 9].

Due to their durability, metal oxides and their composites are useful in fabricating membrane reactors for chemical reactions occurring at very high temperatures such as the dehydrogenation of alkanes and the steam reforming of methane and alcohols [10]. In addition, membranes fabricated from ZrO_2 composites can offer stable performance under alkaline reaction conditions [11]. Sintering, however, is a major problem for the long-term utility of metal oxides as catalytic membrane supports [12]. In heterogeneous catalysis, reacting species are required to diffuse and adsorb to and products need to desorb from the surface of catalysts where the reaction occurs. Therefore, the effective surface area of such catalysts/supports has become an important factor in the provision of adequate reaction sites that allow high levels of conversion. Unfortunately, exposure of catalysts/supports to high temperatures for extended periods of time leads to sintering. In crystalline ceramics, sintering is a process that leads to a loss of porosity where porous materials are transformed into dense polycrystalline aggregates during heating [13].

Lin et al. defined the thermal stability of a ceramic membrane as the ability to retain its phase, mechanical strength, and pore structure—or only to change negligibly—at a given temperature for an extended period of time [14]. His group had previously found that the phase transformation of certain ceramic oxides (Al_2O_3, ZrO_2 and TiO_2) occurred at certain temperatures [15]. Further increase in the heat treatment temperatures resulted in grain growth of the new crystalline phase. These phase transformations and grain growth significantly alter the material pore structure, and lead to a reduction in the surface area and pore volume. Mercera et al. [16] and Shi et al. [17] demonstrated that doping La_2O_3 into Al_2O_3 and doping Y_2O_3 into ZrO_2 were effective in stabilizing them against phase transformation.

Generally, the strategy for improving the thermal stabilities of ceramic oxides such as Al_2O_3, ZrO_2, and TiO_2 involves either reducing the specific surface energy of the metal oxide crystallites [17] or reducing the concentration of nucleation sites to prevent phase transformation [18]. The concentration of nucleation sites can be reduced by doping a second metal oxide with a cation that possesses a larger ionic radius [14]. Y^{3+} has an ionic radius that is 1.06 Å larger than that of Zr^{4+} (at 0.87 Å). In addition to this, the specific surface energy can be reduced by the addition of a second oxide with a lower sintering rate to cover the surface of the primary oxide. In this sense, titania has been useful in lowering the sintering rate of zirconia [18].

The stability of tetragonal ZrO_2 from phase transformations in silica-zirconia composites prepared via the sol-gel co-condensation of silica and zirconia phases has been reported by other researchers [5, 6, 19]. According to Yoldas [19], a 22% proportion of silica in silica-zirconia composites offers a molecular-level separation of the zirconia phase during co-condensation reactions thereby restricting the formation of large particles. Therefore, the sol-gel synthesis of silica-derived composites offers an alternative route for obtaining phase-stable ceramic composites.

The combinations of SiO_2 with Al_2O_3, ZrO_2, or TiO_2 have been accomplished in the pursuit of different objectives by various membrane research groups. When Al_2O_3, ZrO_2, and TiO_2 are used as the primary oxides, silica is introduced either to improve phase stability [19] or to tune the surface acidity/basicity for catalytic purposes [20]. However, when SiO_2 is the primary oxide, ceramic oxides are introduced to stabilize it against pore structure densification [3, 4, 21]. In membrane reactors the preservation of the membrane pore structure and the retention of high levels of membrane permselectivity are of utmost importance.

Our group has developed reproducible colloidal SiO_2-ZrO_2 sols for use in membrane fabrication [5, 6, 21–23]. SiO_2-ZrO_2 has been utilized for the formation of an

intermediate layer between an active membrane separation layer and α-Al_2O_3 particle support and also as the binding agent for α-Al_2O_3 particles. Up to a temperature of 550 °C, TEM and XRD analyses confirmed the presence of amorphous zirconia, but a tetragonal phase began to form at 600 °C and grew in intensity as the calcination temperature increased [5]. The appearance of tetragonal zirconia resulted in a reduction in the effective surface area and pore volume of the composite [22]. Thus, further improvement in the stabilization of zirconia in the amorphous phase at elevated temperatures is desirable. As previously highlighted, yttria (Y_2O_3) stabilization of zirconia is very popular to fabricate dense Y-TZP for fuel cell applications [24, 25]. This creates another problem, however, that of dealing with yttria stability without affecting the microstructural properties.

Therefore, via the colloidal sol-gel route, we propose microstructural control of SiO_2-ZrO_2 composites by doping with yttria. In this work, optimization of the doping ratio of yttrium into the composite was determined via characterization of the sols, film powders, and membranes of yttria-doped SiO_2-ZrO_2 composites. Furthermore, we studied the firing temperatures attained with yttria doping and the effects on the microstructure of the doped composites compared with the undoped variants. Finally, we present long-term performance comparisons of supported membranes derived from doped and non-doped SiO_2-ZrO_2 composites.

2 Experimental

2.1 Materials

The SiO_2-ZrO_2 sols were prepared via the sol-gel process. Tetraethoxysilane (TEOS; Aldrich) was used as the silica precursor while zirconium n-butoxide (ZrTB; Aldrich) served as the zirconia precursor, and each was dissolved in ethanol (EtOH; Aldrich). In the sol-gel reactions, nitric acid (HNO_3; Nacalai Tesque) served as the catalyst for hydrolysis. To obtain yttria-doped SiO_2-ZrO_2 sols, yttrium nitrate hexahydrate ($Y(NO_3)_3.6H_2O$; Aldrich) was utilized. All materials were used as received without further purification.

The SiO_2-ZrO_2 membranes were fabricated on supports. The membrane support was comprised of porous cylindrical α-Al_2O_3 (60% porosity; 1.2 µm pore size; outer diameter, 1 cm; and, length, 10 cm; Nikkato Corporation, Japan).

2.2 Preparation of SiO_2-ZrO_2 and Y-SiO_2-ZrO_2 (Si:Zr 1:1) colloidal sols, powders and membranes

The preparation procedures of pristine SiO_2-ZrO_2 (SZ) and yttria-doped SiO_2-ZrO_2 (Y-SZ) colloidal sols are schematically presented in Fig. S1. The procedure for SZ colloidal sol preparation was reported in our previous work [5, 6, 21–23]. Both types of sols were prepared with a molar ratio of Si to Zr of 1:1. The preparations of all SZ and Y-SZ colloidal sols followed the same basic procedure as the Y-SZ sol preparation initiated by first dissolving $Y(NO_3)_3.6H_2O$ in ethanol mixed at 600 rpm. The amounts of the different materials used are presented in Table S1. Subsequently, TEOS was then introduced and partially pre-hydrolyzed for 3 h after which the required amount of ZrTB was added with water and HNO_3 for co-hydrolysis and co-condensation reactions for another 12 h at room temperature. The co-hydrolysis and co-condensation reactions were then completed afterwards with the addition of more water and HNO_3 to form a polymeric sol after 1 hour. For dilution, water was subsequently added to the polymeric sols to produce a 2 wt % solution. This solution was then boiled for 8 h to form a colloidal sol accompanied by the removal of ethanol and then more water was added to return the concentration at 2 wt%.

Powders used for characterization were prepared from these sols via a quick-drying process whereby the sols were deposited dropwise into a platinum plate heated at 200 °C to generate xerogels that were subsequently calcined at the required temperatures.

The SZ and Y-SZ membranes were fabricated by hot-coating respective SZ and Y-SZ colloidal sols diluted from 2 wt% to 0.5 wt% onto pre-fabricated membrane substrates that had been preheated in an oven at 200 °C. The membrane substrates were comprised of two α-Al_2O_3 layers of different-sized particles fabricated on a cylindrical α-Al_2O_3 support. These layers were prepared by coating a 10 wt% suspension of α-Al_2O_3 particles (diameter 2-3 µm and 0.2 µm particles in the colloidal SZ or Y-SZ sol as a binder) onto the cylindrical α-Al_2O_3 support followed by drying, polishing and calcination at 550 °C. This procedure was repeated for each particle layer to achieve a smooth substrate for subsequent SZ and Y-SZ sol coating.

2.3 Characterization of SiO_2-ZrO_2 and Y-SiO_2-ZrO_2 sols and powders

The particle size distributions of the sols were measured at room temperature via dynamic light scattering (DLS) using a Malvern Zetasizer Nano ZS (Malvern Instruments Ltd.). The changes in the chemical structures of the powders were evaluated via Attenuated Total Reflectance Fourier Transform Infrared Spectroscopy (ATR-FTIR, FTIR-4100, JASCO, Japan). The thermal decomposition properties of samples were analyzed using Thermogravimetry-Mass Spectroscopy (TGA-DTA-PIMS 410/S, Rigaku, Japan; DTG-60 Shimadzu Co., Japan) under He gas flows of 80 ml min^{-1} with a heating rate of 10 °C min^{-1}. Crystallinity in the powders was analyzed via X-ray diffractometry (XRD,

D2 PHASER X-Ray Diffractometer, Bruker, Germany) with Cu Kα as the radiation source at a wavelength of 1.54 Å. The crystalline/amorphous strucutres of the powders were further confirmed by transmission electron microscopy (TEM; JEOL, Japan). The microporosities of the powders were evaluated via N_2 adsorption-desorption experiments at −196 °C (BELSORP MAX, BEL Co., Japan). Prior to this measurement, samples were evacuated of adsorbed gases and vapors at 200 °C for at least 12 h. X-ray photoelectron spectroscopy (XPS, Shimadzu, Japan) was used to analyze the chemical changes resulting from the thermal treatment of powders.

2.4 Characterization of SiO_2-ZrO_2 and Y-SiO_2-ZrO_2 membranes and evaluation of membrane performance

The morphologies of the membranes were analyzed using field emission scanning electron microscopy (FE-SEM, Hitachi S-4800, Japan). Prior to examination, sections were carefully cut from the supported membrane, attached to sample stages via carbon tape, and vacuum dried at 50 °C for 24 h.

The membranes were characterized before and after the long-term thermal stability tests by analyzing the pore size distribution and cross-sectional morphologies of the membranes. The pore size distributions of the membranes were evaluated by nanopermporometry (NPP). The principle of nanopermporometry and details of the measurement can be found in a report by Tsuru et al. [26]. In brief, the distribution of pore sizes in the membranes was determined by the degree of pore blockage by hexane vapor and the effect this exerted on the permeation of nitrogen gas at room temperature. The capillary condensation of hexane in the membrane pores blocks the passage of nitrogen through the membrane. Mixtures of nitrogen gas and hexane vapor in different compositions were made by gradually changing the partial vapor pressures from a pure nitrogen flow until pure hexane flow. These offered the means to evaluate the pore size distribution by measuring the stable nitrogen permeance at each mixing stage and calculating the pore size by the Kelvin equation.. Prior to NPP evaluation, the membranes were preheated in an oven at 200 °C to remove all traces of adsorbed moisture.

The performances of SZ-derived and Y-SZ-derived membranes fabricated at 550 °C were evaluated by observing the long-term N_2 permeance of the membranes at 850 °C. After the fabrication of membranes at 550 °C, respective membranes were installed into the module, which is part of the gas permeation rig. Figure S2 shows the schematic flow diagram of the gas permeation set-up. Nitrogen gas was fed to the upstream side of the membrane module under atmospheric pressure at 850 °C while the downstream section of the membrane module was evacuated using a vacuum pump. The permeance of N_2 through a membrane was evaluated over time by dividing the N_2 permeation rate by the observed transmembrane pressure difference. N_2 permeation rate was obtained by utilizing a pre-calibrated critical nozzle placed between the permeate side and the vacuum pump.

3 Results and discussion

3.1 Characterization and optimization of yttrium doping in SiO_2-ZrO_2

The source of yttrium dopant, $Y(NO_3)_3.6H_2O$, was carefully selected due to its universal solubility in water and alcohols. However, as a result of the need to strictly control the rates of hydrolysis and condensation to form a SiO_2-ZrO_2 colloidal sol with the desired properties, it was important to consider the water of crystallization that was present in the $Y(NO_3)_3.6H_2O$ structure. The presence of 6 moles of water per mole of nitrate requires an adjustment in the calculation of the amount of water necessary for hydrolysis.

To evaluate the effect that the water of crystallization in $Y(NO_3)_3.6H_2O$ exerts on the hydrolysis and condensation reactions, different amounts of yttrium salts were calculated based on different yttrium/zirconium molar ratios (0, 1/9, 2/8, and 3/7), and were then added to the colloidal SZ sols initially prepared with the same amount of water for hydrolysis. The particle sizes of the resultant nitrate-SZ sol mixtures were measured, and the results are presented in Fig. 1. The addition of $Y(NO_3)_3.6H_2O$ to the SZ sols meant that an additional amount of water was now present, which was based on the added amounts of nitrate. Figure 1 compares the increase in sol size from the additions of yttrium nitrate with the sol size without yttrium nitrate added. This

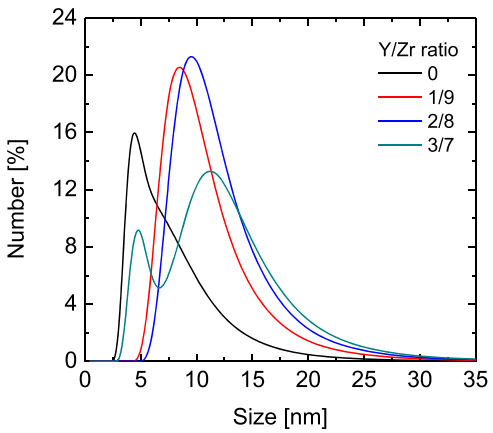

Fig. 1 Particle size distributions of $Y(NO_3)_3.6H_2O$-SiO_2-ZrO_2 colloidal sol mixtures with different yttrium/zirconium molar ratios

shows that the additional water molecules of crystallization introduced by the addition of $Y(NO_3)_3.6H_2O$ induced additional hydrolysis and condensation reactions. At a Y/Zr ratio of 3/7, however, the particle size distribution showed two peaks indicating the bimodal particle size distribution that might have resulted from the onset of yttrium hydrolysis due to the abundance of yttrium ions. Therefore, the water of crystallization in the yttrium salt must be considered when calculating the amount of water required for hydrolysis. To confirm that the increase in particle size distributions was not due to yttrium catalyzation, different colloidal sols were prepared by keeping the water amount constant (including the water of crystallization) while varying the yttrium content from 0 to 20% of added zirconium precursor. As Fig. S3 shows, no significant difference was recorded in the measured particle size distributions of the colloidal sols after a slight decrease in distribution after initial yttrium doping indicating that yttrium ions in isolation did not significantly influence the hydrolysis/condensation reactions, and that the total amount of water is key to controlling the colloidal sol size.

Furthermore, it is important to optimize the amount of yttrium required for the doping of the SZ to achieve the required microstructural benefits. The objective is to dope the SZ microstructure with yttrium in its ionic state. As pointed out earlier and shown in Fig. 1, the amount of added $Y(NO_3)_3.6H_2O$ can also determine the eventual state of yttrium in the resultant Y-SZ sol. At a Y/Zr ratio of 3/7, the bimodal particle size distribution emanating from a possible yttrium hydrolysis will eventually lead to the premature presence of crystalline yttria (Y_2O_3) phase after calcination, which could have a negative effect on the SZ microstructure. The yttrium amount was optimized by observing

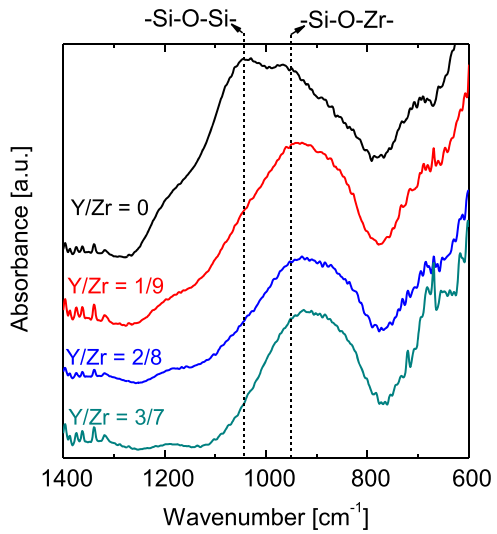

Fig. 2 ATR-FTIR spectra of $Y\text{-}SiO_2\text{-}ZrO_2$ powders with different yttrium/zirconium molar ratios all prepared at 550 °C

the effect of Y/Zr ratios of 1/9, 2/8, and 3/7 on the microstructural properties of Y-SZ by FTIR, XRD, XPS, and N_2 adsorption. It should be noted that the colloidal sols used in forming the characterization films and powders were prepared by considering the amount of water of crystallization in the yttrium nitrate along with the water needed for hydrolysis.

First, the effect of the yttrium doping on the bonding structure was evaluated via FTIR. Figure 2 shows the ATR-FTIR spectra ranging from 1,400 to 600 cm^{-1} for $Y\text{-}SiO_2\text{-}ZrO_2$ powders with different yttrium/zirconium molar ratios. As shown by the profile of the pristine SZ powder, the peaks for –Si–O–Si– bonds appear at 1,050 cm^{-1} as a result of the network configuration of siloxane [27]. The shoulder appearing at approximately 970 cm^{-1}, however, represents the occurrence of –Si–O–Zr– bonds [28]. Subsequent to doping with yttrium, as shown in Fig. 2, the occurrence of the -Si-O-Si- bond continued to range between 750 and 1,250 cm^{-1}. Peaking at a lower wavenumber of 925 cm^{-1} usually indicates the formation of more –Si–O–Zr– bonds [28]. This observation is true irrespective of the Y/Zr molar ratio, which suggests that the utilization of yttrium facilitates a more homogeneous dispersion of the $SiO_2\text{-}ZrO_2$ composition. Also, the yttrium amounts corresponding to Y/Zr molar ratios of 2/8 and 3/7 may not be required if a Y/Zr ratio of 1/9 is adequate to achieve the required network modification. This is true particularly because the utilization of a higher amount of yttrium in the doping process risks the formation of a separate unwanted yttria phase. Further characterizations were thus necessary to confirm the adequacy of a Y/Zr molar ratio of 1/9.

Figure 3 shows the XRD patterns of Y-SZ powders with different Y/Zr molar ratios fired at 600 and 800 °C. This was previously established based on XRD and TEM observations in several studies by our group [5, 6, 22] showing that pristine $SiO_2\text{-}ZrO_2$ remains amorphous after calcination at 550 °C. Puthai et al. [5] reported that the aggregation of ZrO_2 into the tetragonal phase commenced between 600 and 650 °C. Figure 3a confirms this observation. The XRD pattern of an SZ sample calcined at 600 °C with no yttrium doping (Y/Zr = 0), as shown in Fig. 3a, has the appearance of a small peak representative of a tetragonal ZrO_2 (t-ZrO_2) phase at 2θ of 30.1°. With the doping of yttrium, however, perfect amorphousness is retained with no crystalline peaks observed at Y/Zr ratios of 1/9, 2/8 or 3/7, as shown by Fig. 3a. This indicates a successful prevention of the crystal-phase formation that would have otherwise formed without yttrium doping. Nonetheless, at a Y/Zr ratio of 3/7 (Fig. 3a), the shape of the broad amorphous hump ranging between 2θ of 20 and 40 ° tends to skew towards a lower 2θ typically in the position associated with the occurrence of a yttria phase. Therefore, the onset of yttria-phase aggregation is highly likely.

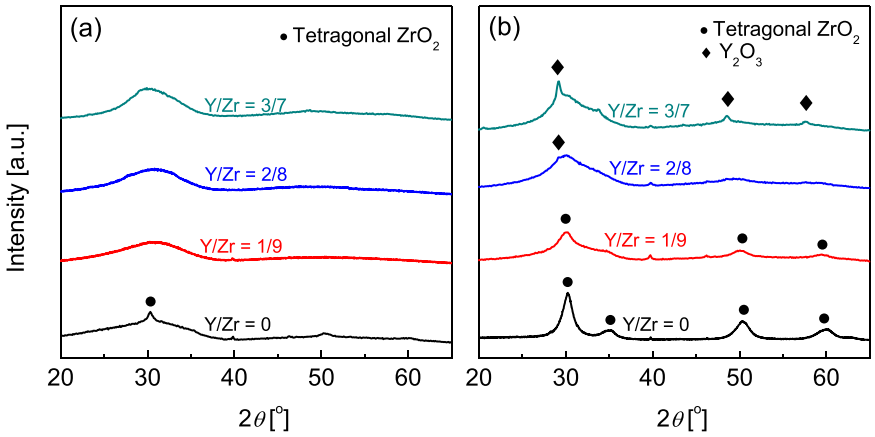

Fig. 3 XRD patterns of Y-SiO_2-ZrO_2 gels with different yttrium doping ratios fired at (**a**) 600 °C and (**b**) 800 °C under an air atmosphere

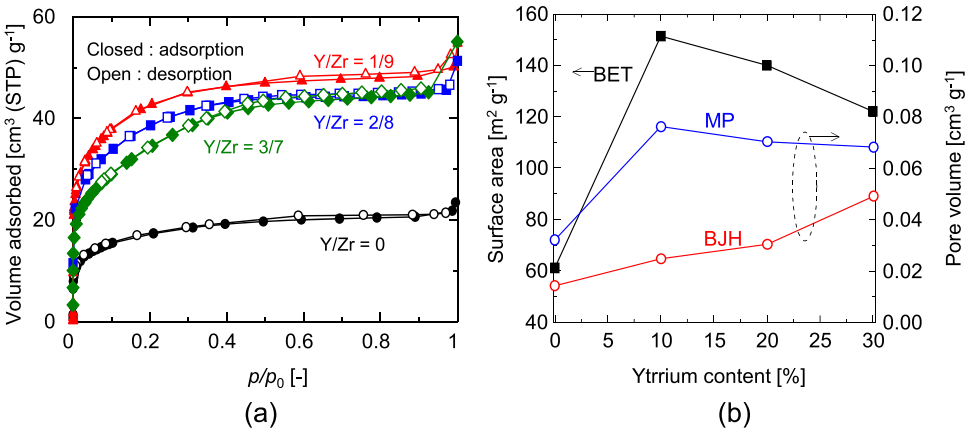

Fig. 4 **a** N_2 adsorption-desorption isotherms at −196 °C of Y-SiO_2-ZrO_2 powders with different yttrium contents calcined at 550 °C (**b**) surface areas, micropore and mesopore volumes of Y-SiO_2-ZrO_2 (Si/Zr = 5/5) powders as a function of yttrium content

A comparison of Fig. 3a, b at each Y/Zr ratio, shows that a dramatic change in the phases occurs after calcination at 800 °C. At a Y/Zr ratio of 0, the aggregation of t-ZrO_2 became more severe with additional occurrences at 2θ of 35, 50.3 and 60.1°, which is indicative of the sintering process of t-ZrO_2. The Y/Zr ratio of 1/9 showed similar occurrences of t-ZrO_2 growth at 2θ of 30.1, 50.3, and 60.1°, albeit to a much lesser degree than without the yttrium doping. Increasing the yttrium doping amount beyond a Y/Zr ratio of 1/9 resulted in suppression of the t-ZrO_2 phase even at a severely high temperature of 800 °C. However, the appearance of yttria can be observed with a peak occurrence at 29°, the growth of which increased when the Y/Zr ratio was increased to 3/7 (Fig. 3b) with the additional occurrences at 2θ of 48.5 and 56.7°. Therefore, the choice of the yttrium doping amount that provided the least trade-off of t-ZrO_2 phase suppression with no yttria phase formation proved to be a Y/Zr ratio of 1/9.

In Fig. 4a, the N_2 adsorption-desorption isotherms measured at −196 °C for the Y-SZ powders with different yttrium contents are shown. The adsorption measurements were carried out for powders calcined at 550 °C at which all samples can be considered to be amorphous via proper characterization. Figure 4b and Table 1 summarize the

Table 1 Summary of N_2 adsorption–desorption results for Y-SiO_2-ZrO_2 powders with different yttrium contents

Y/Zr ratio	S_{BET} [$m^2\ g^{-1}$]	V_{MP} [$10^{-3}\ cm^3\ g^{-1}$]	V_{BJH} [$10^{-3}\ cm^3\ g^{-1}$]
0	61.1	32.2	14.3
1/9	151	76.2	24.8
2/8	140	70.4	30.5
3/7	122	68.3	49.2

S_{BET} Specific surface area, V_{MP} Micropore volume, V_{BJH} Mesopore volume

derived measurements of BET (Brunauer-Emmett-Teller) specific surface areas, MP specific micropore volumes, and BJH (Barrett-Joyner-Halenda) specific mesopore volumes as a function of yttrium content. First, the adsorption-desorption isotherms showing the amount of N_2 adsorbed reveal that the microporous structure of SiO_2-ZrO_2 was modified by doping with yttrium. Particularly, the doping of SZ with yttrium at a Y/Zr ratio of 1/9 increased the amount of N_2 adsorbed, which indicated that yttrium incorporation prevented both the densification of the silica phase and the aggregation of the zirconia phase, which are usually the causes of low porosity in SiO_2-ZrO_2 composites [20, 22, 28]. After the initial increase in adsorbed N_2, a further increase in

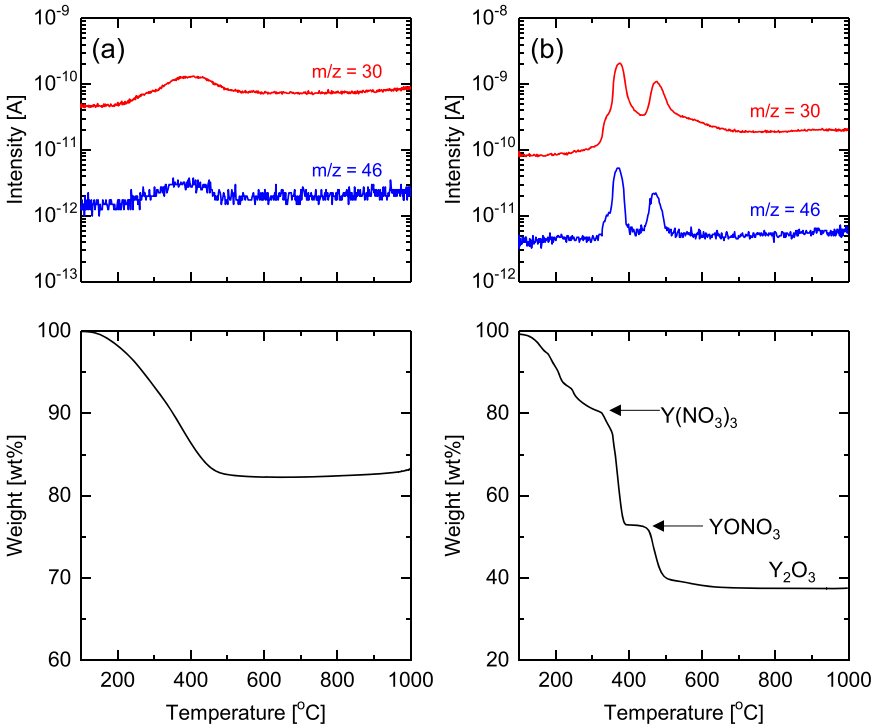

Fig. 5 TG-curve and mass spectra of (**a**) Y-SiO_2-ZrO_2 (Y/Zr = 1/9) and (**b**) $Y(NO_3)_3.6H_2O$ gels under a He/O_2 atmosphere

the yttrium content from a Y/Zr ratio of 1/9 to 2/8 and then to 3/7 resulted in a decrease in the amount of N_2 adsorbed.

Figure 4b reveals more information on this trend. The trend of the BET-derived specific surface area is similar to that observed for the amount of N_2 adsorbed. An initial increase in the BET surface area from 61.1 to 151 $m^2\ g^{-1}$ after doping with a Y/Zr ratio of 1/9 was followed by decreases to 140 and 122 $m^2\ g^{-1}$ after increasing the yttrium doping amounts to Y/Zr ratios of 2/8 and 3/7, respectively. The shapes of the isotherms suggest a type 1b IUPAC classification (a steep uptake of adsorbent at low p/p_0 and limited uptake for higher p/p_0), which means the samples could be comprised of micropores and narrow mesopores [29, 30]. The micropore volume was evaluated using the micropore analysis method (MP) while the mesopore volume was evaluated via the BJH method. The micropore volumes also showed a trend similar to that of BET-derived surface areas. Therefore, it would be plausible to assume that the amount of N_2 adsorbed by these samples is likely to be determined primarily by the micropore volume. The mesopore volumes, on the other hand, increased with an increase in the yttrium content. In particular, despite the lower surface area exhibited by the Y-SZ sample with a Y/Zr ratio of 3/7, the mesopore volume was drastically increased, which indicated that the generation of phase-separated yttria had a deleterious effect on the surface area. From the results in the present study, the yttrium doping amount corresponding to a Y/Zr molar ratio of 1/9 can be conclusively regarded as adequate for effecting the necessary microstructural control without the risk of yttria phase aggregation.

The presence of yttrium in an ionized state after doping with a Y/Zr ratio of 1/9 was confirmed by thermogravimetry-mass spectroscopy (TG-MS) and x-ray photoelectron spectroscopy (XPS). Figure 5a shows the TG curves and decomposition mass spectra of Y-SZ with a Y/Zr ratio of 1/9. The onset of decomposition can be observed from about 150 °C and completed at 500 °C. The mass spectra analyzed for this decomposition reveal mass peaks corresponding to m/z values of 30 and 46. To determine the chemical composition of the volatile decomposition products of Y-SZ, the TG curve and mass spectra of $Y(NO_3)_3.6H_2O$ decomposition were obtained for comparison and are shown in Fig. 5b. Here the loss of the water of crystallization occurred between 150 and 350 °C. Subsequent to this, a sharp loss of mass occurred with a corresponding mass peak appearing between 350 and 390 °C. These mass losses correspond to m/z values of 30 and 46, and are assigned to the loss of NO_x volatile species NO and NO_2, respectively [31]. Hence, $YONO_3$ could be considered the chemical state of the residual material between 390 and 450 °C. Further decomposition then occurs at an elevated temperature range of 450 to 650 °C before forming a final yttria (Y_2O_3) phase. In contrast to the decomposition mass spectra of $Y(NO_3)_3.6H_2O$, the decomposition of Y-SZ (Fig. 5a) shows a mass spectra with only a single broad signal suggesting that the loss of volatile NO and NO_2 species occurred simultaneously from the dissociated NO_3^- ions contained in the freshly prepared Y-SZ sample. This points to

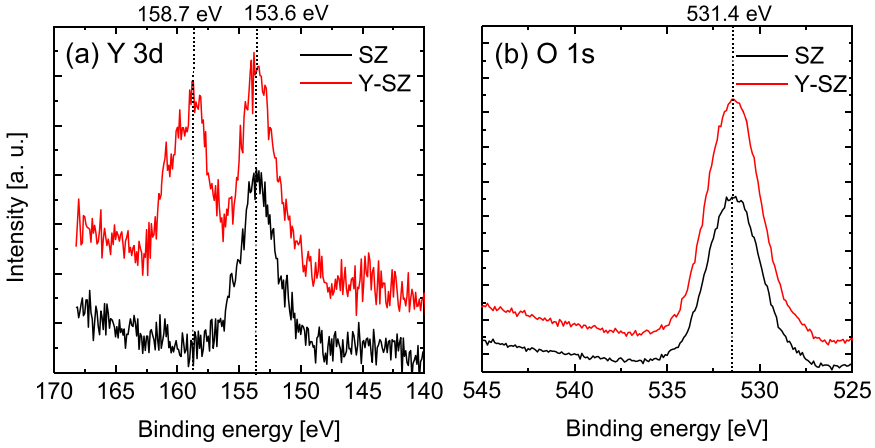

Fig. 6 Narrow x-ray photoelectron spectra (XPS) of (**a**) yttrium Y 3d and (**b**) oxygen O 1 s for Y-doped and undoped SiO_2-ZrO_2 powders prepared at 550 °C under an air atmosphere

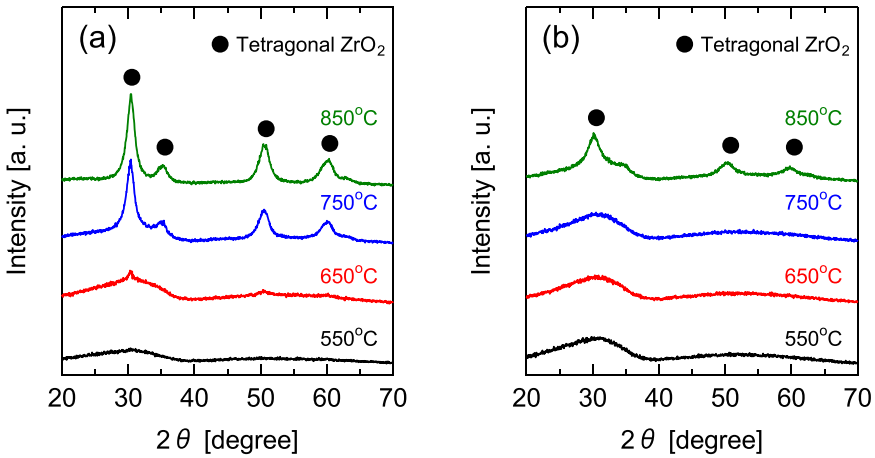

Fig. 7 XRD patterns of (**a**) SiO_2-ZrO_2 (Si/Zr = 5/5) and (**b**) Y-SiO_2-ZrO_2 (Si/Zr = 5/5, Y/Zr = 1/9) gel calcined under air at various temperatures

the transformation of the nitrate to yttrium ions during the calcination process.

Furthermore, via the use of XPS to observe the elemental presence of yttrium and its effect on the oxygen spectra, we were able to determine the status of yttrium since the formation of the yttria phase would cause a shift in the oxygen spectra compared with pristine SZ. Figure 6a shows the narrow Y 3d spectra of pristine SZ (black) and Y-SZ (red) samples following calcination at 550 °C. The common peak at 153.6 eV is usually assigned to the $3d_{5/2}$ photoelectron state of yttrium and could be ascribed to measurement inaccuracy associated with the atomic proximity of yttrium (atomic number 39) and zirconium (atomic number 40) [32]. Nonetheless, the presence of yttrium was clearly identified in the Y 3d spectrum of Y-SZ, which showed a peak at 158.7 eV representing a photoelectron state of $3d_{3/2}$ [32] that does not appear in pristine SZ. However, when comparing the narrow O 1 s spectra of both samples, as shown in Fig. 6b, the peaks showed no difference in either their position or their shape. Hassan et al. [33] incorporated copper into silica-zirconia and discovered a change in the O 1 s photoelectron lines due to the formation of Zr-O-Cu bonds. This indicates that the presence of yttrium has a negligible influence on the O electronic environment, and, hence, promotes the assumption of an ionic yttrium state.

3.2 Evaluating the contribution of Yttrium-doping to the microstructural stability of SiO_2-ZrO_2 composites during thermal treatment

Although previous discussions have established that doping yttrium into SiO_2-ZrO_2 in an amount corresponding to a Y/Zr ratio of 1/9 is effective in suppressing the aggregation of t-ZrO_2, it remains necessary to evaluate the thermal stability threshold of such Y-SZ samples and the changes in the chemical and textural properties during thermal treatment.

Figure 7a, b show the XRD patterns of SZ and Y-SZ powders, respectively, calcined at various temperatures and measured at room temperature. In both figures, it is instructive to note that there was no appearance of Y_2O_3 peaks at any calcination temperature due to the low amount of yttrium doped. In Fig. 7a, as mentioned earlier, the SZ sample calcined at 550 °C shows an amorphous pattern and the onset of t-ZrO_2 aggregation occurs at 650 °C with a peak at 2θ of 30.1° indicating a low stability threshold. At

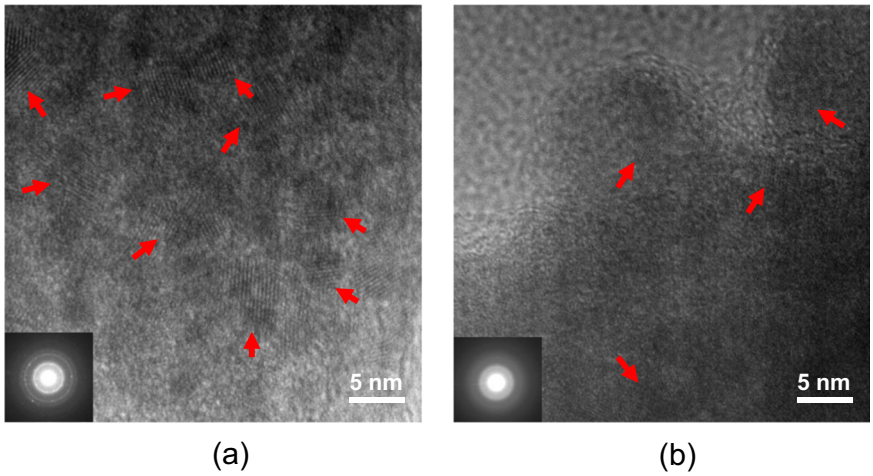

Fig. 8 High-resolution transmission electron microscopy (HRTEM) images of (**a**) SiO_2-ZrO_2 and (**b**) Y-SiO_2-ZrO_2 calcined at 850 °C (Inset: Selected Area Electron Diffraction images)

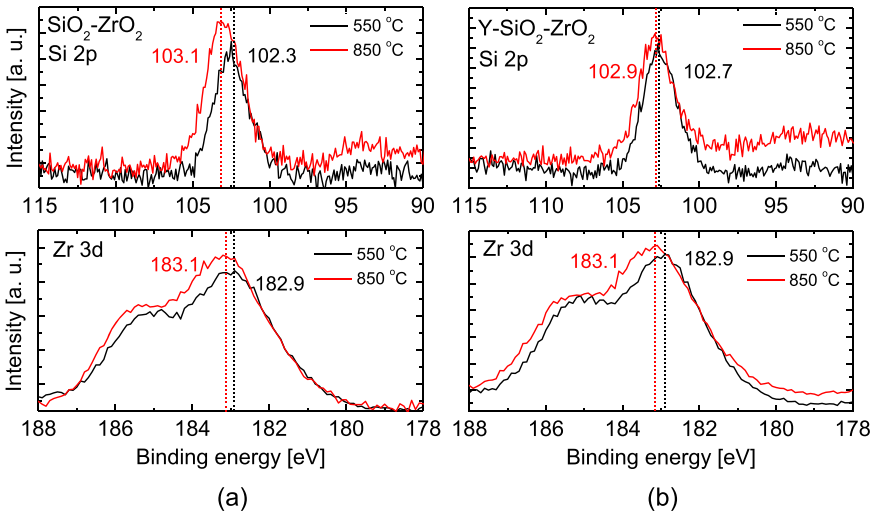

Fig. 9 Narrow Si 2p and Zr 3d XPS spectra of (**a**) SiO_2-ZrO_2 and (**b**) Y-SiO_2-ZrO_2 composite powders fired at 550 and 850 °C

750 °C, an accelerated growth of the t-ZrO_2 crystals occurs, as shown by the appearance of multiple peaks at 2θ of 30.1 35, 50.3, and 60.1°. The growth of the t-ZrO_2 crystals continued at 850 °C. The approximate crystal sizes were calculated according to Scherrer's equation, which appears in Table S2 and agrees with calculations by Liu et al. [34]. This indicates that the calcination temperature is a driving factor in the mechanism for the aggregation of t-ZrO_2 crystals. According to Hishita and co-workers [35], calcination temperature causes nanoparticles to be attracted to nucleation sites, which results in crystal growth with increasing temperature.

On the other hand, the yttrium-doped sample displayed a higher degree of thermal stability. According to Fig. 7b, an amorphous phase was maintained up to 750 °C. Compared with pristine SZ, there was no apparent aggregation of t-ZrO_2 crystals at 750 °C. However, t-ZrO_2 peaks suddenly appeared at 850 °C, but the intensity of these peaks in the Y-SZ pattern at 850 °C was weaker than that of pristine SZ. According to Lin et al. [14], Y^{3+} ions with ionic radii larger than that of Zr^{4+} are able to shield it from thermal diffusion. Hence, the doping of yttrium at a Y/Zr ratio of 1/9 stabilizes SiO_2-ZrO_2 up to 750 °C.

After calcination of the samples at 850 °C, it was apparent that the t-ZrO_2 peaks appearing in the XRD patterns for the pristine SZ sample showed higher intensity compared with those of the Y-SZ sample. The t-ZrO_2 crystallite size detailed in Table S1 was calculated at 6.5 nm for the SZ sample compared with 4.5 nm for the Y-SZ sample. The crystallite size, however, may not provide an accurate representation of the degree of aggregation. Figure 8a, b show the HRTEM images of SZ and Y-SZ samples after calcination at 850 °C, respectively. On a scale of 5 nm, the crystal structures can be identified by the clustering of patterns with closely knitted grain boundaries, which represents an ordered crystalline lattice. Figure 8a shows the high density of these lattice clusters of aggregated t-ZrO_2 in a pristine SZ sample. For the Y-SZ sample, however, Fig. 8b shows that the density of the lattice patterns is less severe, which suggests a suppression of the aggregation of t-ZrO_2 crystals. Additionally, selected area electron diffraction (SAED) images (shown in the inset)

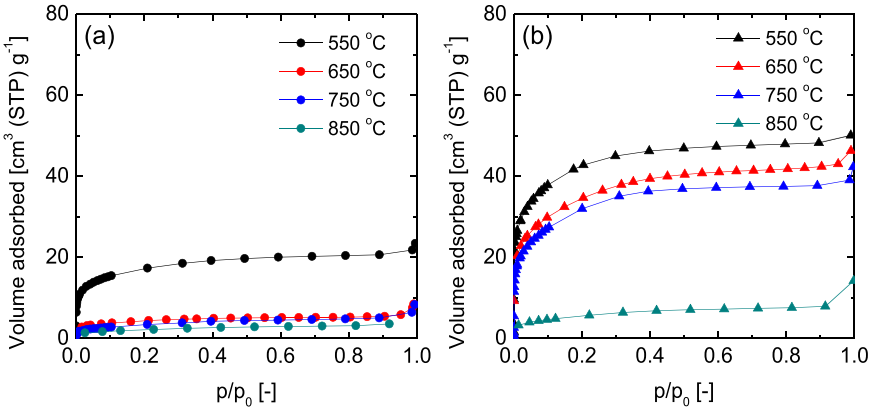

Fig. 10 N_2 adsorption isotherms at 77 K of (**a**) SiO_2-ZrO_2 and (**b**) Y-SiO_2-ZrO_2 powders calcined under air at various temperatures

Table 2 Summary of N_2 adsorption parameters for SiO_2-ZrO_2 and Y-SiO_2-ZrO_2 powders calcined under air at various temperatures

Calcination temperature [°C]	SiO_2-ZrO_2		Y-SiO_2-ZrO_2	
	S_{BET} [$m^2\ g^{-1}$]	V_{MP} [10^{-3} $cm^3\ g^{-1}$]	S_{BET} [$m^2\ g^{-1}$]	V_{MP} [10^{-3} $cm^3\ g^{-1}$]
550	63.7	32	158	76
650	15.6	7.3	124	65
750	11.8	6.2	116	59
850	7.51	4.2	20.9	11

clearly reveal ring and dot patterns in the pristine SZ sample, which supports a high level of crystalline intensity. The SAED image of the Y-SZ sample shows mostly a halo and ring pattern that represents weaker crystalline intensity.

The XRD and TEM data clearly show changes in the microstructural states of the pristine SZ and Y-SZ samples following exposure to high temperatures. These changes are the result and manifestation of the rearrangement of atoms being driven by high temperature. The changes in the states of atoms can be observed by XPS. The narrow Si 2p and Zr 3d spectra for the pristine SZ and the Y-SZ samples calcined at 550 and 850 °C, respectively, are shown in Fig. 9a, b. A pure SiO_2 sample gave a standard photoelectron peak of Si 2p between 103.2 and 103.7 eV [33, 36, 37] while pure ZrO_2 indicated photoelectron peaks of $3d_{5/2}$ and $3d_{3/2}$ at 181.9–182.5 eV and 184.3–184.7 eV, respectively [32, 36–38]. Compared with the pure standard references, the observed Si 2p binding energies (BE) for both pristine SZ and Y-SZ composites calcined at 550 °C showed lower values of 102.3 and 102.7 eV, respectively. This is explained by the higher electronegativity of Si compared with that of Zr whereby the valence electrons on the O atom in an –Si–O–Zr– linkage are attracted more to the Si atom than to Zr, which results in a reduction state with lower BE [38, 39]. The Zr $3d_{5/2}$ peak BE for both samples prepared at 550 °C of 182.9 eV were expected to be higher than the upper value of the reported standard reference due to the diminished electronegativity of Zr, which resulted in an oxidized state with higher BE. This observation agrees with the conclusion that the highly composite nature of the SiO_2-ZrO_2 microstructure would be expressed as XRD amorphous following calcination at 550 °C. Moreover, the chemical vapor deposition (CVD) of zirconium alkoxide on a silica substrate without reactive interaction showed negligible shifts in the Si 2p and Zr 3d peaks even as the Zr loading was increased compared with that of pure SiO_2 and ZrO_2 [40].

Thus, changes in the chemical state following calcination at 850 °C for both pristine SZ and Y-SZ samples could be discussed using observations of the shifts in the BE. Figure 9a, b clearly show exactly the same chemical shift of 0.2 eV for the respective Zr $3d_{5/2}$ peaks at 182.9 eV for both SZ and Y-SZ following calcination at 850 °C. First, a similar amount of chemical shift was expected, as shown in Fig. 7a, b, because the formation of t-ZrO_2 was evident at 850 °C albeit to different degrees. Second, the shift to a higher BE is ascribed to a correlation between the photoelectron state of Zr and the effective ionic valence of Zr atoms. According to Tsunekawa and co-workers, the BE of Zr $3d_{5/2}$ increased with an increase in the effective ionic valence of the Zr atoms. The effective ionic valence measured for Zr atoms was increased with the phase transition of the ZrO_2 crystals calcined from 425 to 1,025 °C [41].

The positive effect of yttrium doping appears in the ability of the Si atom to retain its chemical state as much as possible after 850 °C calcination of the Y-SZ sample. The chemical shifts in the Si 2p peaks reveal that the Y-SZ sample only shifted by a magnitude of 0.2 eV while that of the pristine SZ sample shifted by as much as 0.8 eV, as shown in Fig. 9a, b. This may have been either a result of spill-over or a lack of aggregation in the zirconia phase of the Y-SZ sample. Thus, the silica phase is able to retain much of its chemical and microstructural properties even after the calcination of Y-SZ at 850 °C.

Figure 10a, b show the N_2 adsorption isotherms of pristine SZ and Y-SZ samples, respectively, calcined at different temperatures. The obtained derivable textural properties are summarized in Table 2. Figure 10a shows that

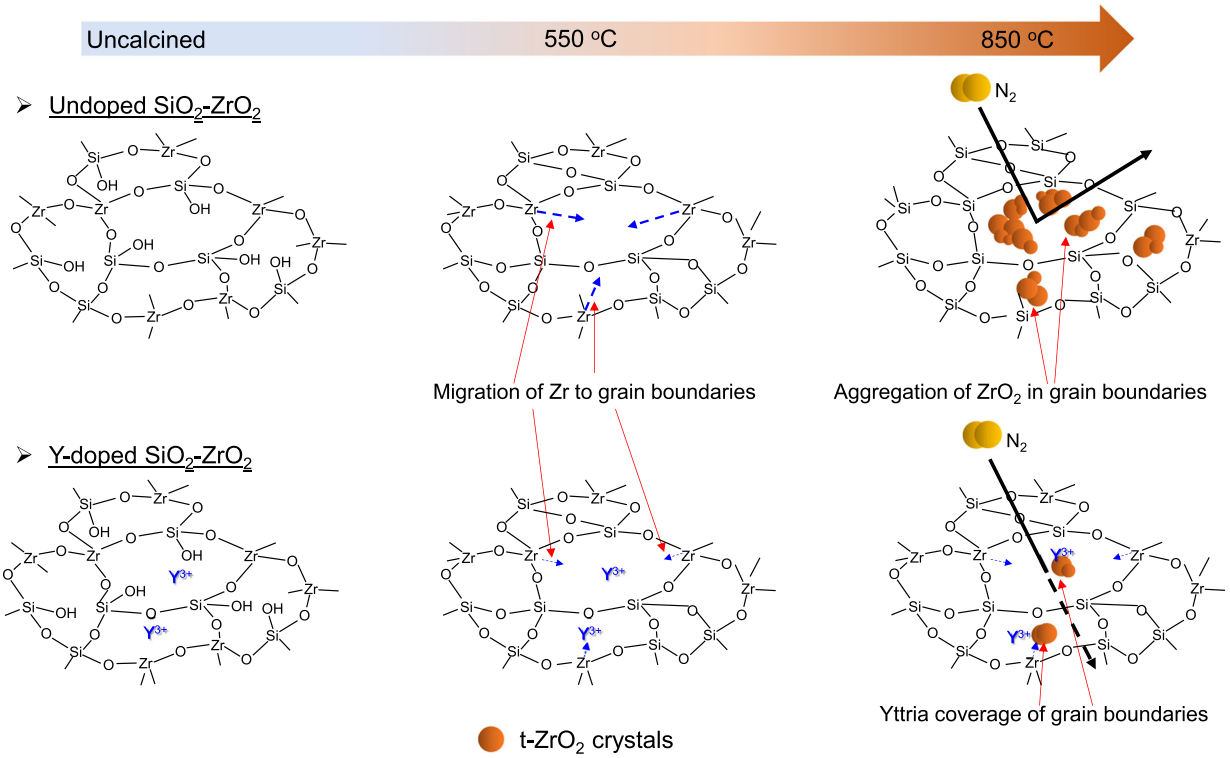

Fig. 11 Schematic images of SiO_2-ZrO_2 and Y-SiO_2-ZrO_2 composite network calcined at different temperatures

the amount of N_2 adsorbed was drastically reduced as the calcination temperature of the SZ sample increased from 550 to 650 °C. The evaluated BET surface area (Table 2) was reduced by 76% upon calcination at 650 °C and by 81% at 750 °C. By contrast, the Y-SZ sample continued to show a very high amount of N_2 adsorbed up to a calcination temperature of 750 °C. Correspondingly, the BET surface area was reduced by only 27%, which subsequently was reduced from 116 to 20.9 $m^2\ g^{-1}$ (82%). Nonetheless, at a calcination temperature of 850 °C, the specific surface area and micropore volume of the Y-SZ sample was still more than double that of the pristine SZ sample. This supports the notion that in the yttrium-doped sample, the prevention of aggregation of the t-ZrO_2 allowed the SiO_2-ZrO_2 phase to retain its microstructural properties at higher calcination temperatures.

Figure 11 summarizes the mechanism for the thermal stability of the SiO_2-ZrO_2 microstructure via yttrium doping. During the calcination of the pristine SZ structure, Zr atoms are predisposed to thermal diffusion in the absence of yttria resulting in the aggregation of ZrO_2. Further calcination results in grain growth in ZrO_2 into denser crystals. Therefore, the separation of SiO_2 and ZrO_2 into separate phases results in an overall reduction in pore volume and surface area, as shown by N_2 adsorption. On the other hand, due to the larger ionic radius of Y^{3+} over Zr^{4+} in Y-SiO_2-ZrO_2, yttria effectively covers the grain boundaries thereby reducing the concentration of the nucleation sites and increasing the activation energy for diffusion [14, 35, 42]. Thus, the surface diffusion of atoms is minimal and results in minimal change in the microstructural properties.

3.3 Evaluation of the long-term performance of a Y-SiO_2-ZrO_2 membrane

The results of several characterizations provided evidence that yttrium doping into SiO_2-ZrO_2 yields microstructural benefits for thermal stability. However, since the eventual applications of Y-SZ composites are in membrane reactors or gas separation membranes, it was necessary to characterize and compare the performance of SZ- and Y-SZ-derived supported membranes. First, the successful preparation and retention of membranes was established via scanning electron microscopy (FE-SEM) of the membrane cross-sections. Figure 12a to d show the SEM images of the cross-sections of SZ and Y-SZ membranes fabricated at 550 and 850 °C. Figure 12a, for example, shows that the membranes were successfully fabricated on 0.2 and 2–3 µm α-Al_2O_3 supports with thicknesses of approximately 200 nm. Therefore, irrespective of the exposure temperature, the membrane morphologies were found to be intact.

Figure 13a, b compare the long-term N_2 permeance stability of SZ and Y-SZ membranes, respectively. Both membranes were initially fabricated at 550 °C with the permeance of N_2

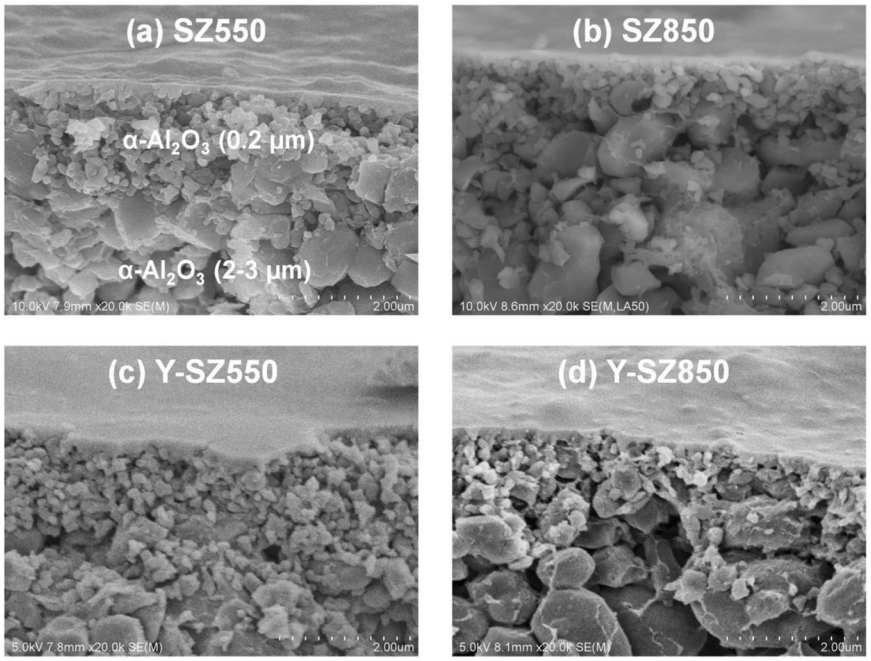

Fig. 12 SEM images of the cross-sections of SiO_2-ZrO_2 membranes fabricated at (**a**) 550 and (**b**) 850 °C; and, Y-SiO_2-ZrO_2 membranes fabricated at (**c**) 550 and (**d**) 850 °C

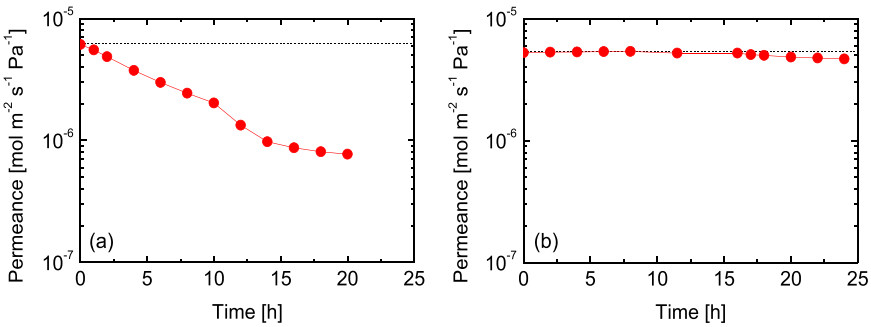

Fig. 13 Time course of N_2 permeance at 850 °C for (**a**) SiO_2-ZrO_2 and (**b**) Y-SiO_2-ZrO_2 membranes prepared at 550 °C

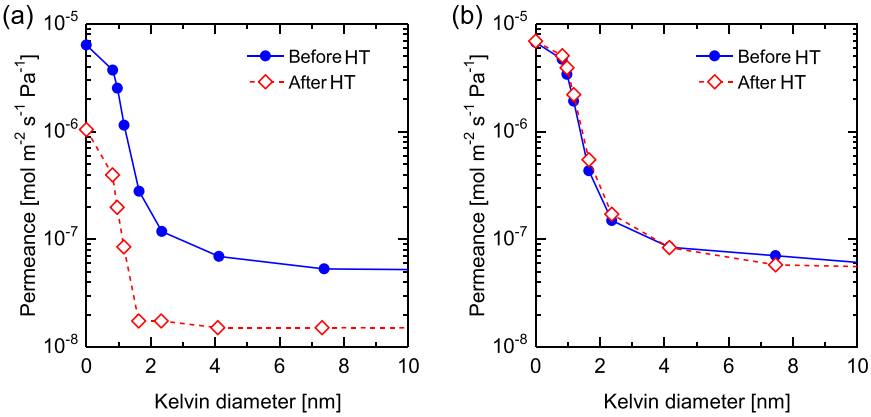

Fig. 14 Nitrogen permeance as a function of the Kelvin diameter of (**a**) SiO_2-ZrO_2 and (**b**) Y-SiO_2-ZrO_2 membranes before and after heat treatment (HT) at 850 °C, as measured via nanopermporometry (vapor: hexane)

measured for an extended time interval at 850 °C. As shown in Fig. 13a, the SZ-derived membrane showed an initial N_2 permeance of 6×10^{-6} mol m^{-2} s^{-1} Pa^{-1}. Shortly after, the permeance of N_2 began to reduce sharply with permeation time. This indicates a reduction in the porosity of the membrane with exposure time. A reduction of the porosity of the membrane at 850 °C is consistent with the idea of densification (reductions in the surface area and pore volume) of pristine SZ observed from N_2 adsorption, as discussed in Section 3.2. According to Chang and co-workers, prior to densification by structural phase transformation, sintering occurs concomitant with changes in the pore structure and densification [15]. This could explain the

early reduction in the N_2 permeance because phase transformation to t-ZrO_2 at 850 °C might not have been immediately possible.

On the other hand, the Y-SZ membrane showed steady N_2 permeance of 5.5×10^{-6} mol m^{-2} s^{-1} Pa^{-1} for up to 16 h of exposure after which a slight reduction to about 5×10^{-6} mol m^{-2} s^{-1} Pa^{-1} occurred and remained stable at this value. Therefore, yttrium doping of SiO_2-ZrO_2 was very effective in preventing the sintering process from reducing the pore size of a Y-SZ membrane. Figure 14a, b show the variations in N_2 permeance in a nanopermporometry experiment as a function of the Kelvin diameter for SZ and Y-SZ membranes before and after heat treatment (HT) at 850 °C. Following HT at 850 °C, the permeance of nitrogen through the SZ membrane was decreased as the Kelvin diameter increased while that of the Y-SZ membrane retained a similar permeance relationship with Kelvin diameter before and after HT at 850 °C. This clearly indicates a loss in porosity in the pristine SZ membrane.

The change in pore size can be evaluated by comparing the normalized permeance of N_2 as a function of Kelvin diameter based on Fig. 14a, b. Figure S4a, b show the dimensionless N_2 permeance as a function of the Kelvin diameter for SZ and Y-SZ membranes before and after HT at 850 °C. Figure S4a shows that at higher Kelvin diameters, the dimensionless N_2 permeance was increased, which indicates that despite the lower porosity of the pristine SZ membrane after HT, the pore size was enlarged. On the other hand, the dimensionless N_2 permeance dependency on Kelvin diameter observed for the Y-SZ membrane remained comparable before and after HT, which indicated no change in the pore size. Based on these results, a Y-SZ membrane significantly showed greater stability than a pristine SZ membrane. Thus, correlations can be established between yttrium doping and its effect on membrane microstructure and performance.

4 Conclusions

In this work, we utilized yttrium doping to achieve a SiO_2-ZrO_2 composite membrane that would be microstructurally stable at temperatures reaching 850 °C. The doping of SiO_2-ZrO_2 with yttrium was accomplished by first applying Y $(NO_3)_3.6H_2O$ salt in a sol-gel reaction procedure. Doped and pristine forms of SiO_2-ZrO_2 were compared via several characterization methods to establish the optimum yttrium amount for doping, the effect of yttrium doping on the thermal stability of Y-doped SiO_2-ZrO_2, and, finally, the long-term membrane performances.

We established that doping with a Y/Zr molar ratio of 1/9 was optimal to prevent the unwanted yttria phase formation that results from excess yttrium doping. The resultant Y-doped SiO_2-ZrO_2 membrane was improved microstructurally and was thermally stable. Finally, Y-doped SiO_2-ZrO_2 membranes proved to be suitable for use in high-temperature reactors and for use as separation membranes.

Acknowledgements The authors appreciate the kind help of Dr. Maeda of the Natural Science Center for Basic Research and Development, Hiroshima University (N-BARD), for his assistance in obtaining the TEM images.

Compliance with ethical standards

Conflict of interest The authors declare no competing interests.

Publisher's note Springer Nature remains neutral with regard to jurisdictional claims in published maps and institutional affiliations.

References

1. Leenars AFM, Keizer K, Burggraaf AJ (1984) The preparation and characterization of alumina membranes with ultra-fine pores: Part 1 Microstructural investigations on non-supported membranes. J Mater Sci 19:1077–1088
2. Burggraaf AJ, Keizer K, van Hassel BA (1989) Nanophase ceramics, membranes and ion implanted layers. Surf. Interf. Ceram. Mater. 705–724
3. Choi H-S, Ryu C-H, Hwang G-B (2013) Obtention of ZrO_2-SiO_2 hydrogen permselective membrane by chemical vapor deposition method. Chem Eng J 232:302–309
4. Ahn S-J, Takagaki A, Sugawara T, Kikuchi R, Oyama ST (2017) Permeation properties of silica-zirconia composite membranes supported on porous alumina substrates. J Membr Sci 526:409–416
5. Puthai W, Kanezashi M, Nagasawa H, Wakamura K, Ohnishi H, Tsuru T (2016) Effect of firing temperature on the water permeability of SiO_2–ZrO_2 membranes for nanofiltration. J Membr Sci 497:348–356
6. Asaeda M, Sakou Y, Yang J, Shimasaki K (2002) Stability and performance of porous silica-zirconia composite membranes for pervaporation of aqueous organic solutions. J Membr Sci 209:163–175
7. Amanipour M, Babakhani EG, Safekordi A, Zamaniyan A, Heidari M (2012) Effect of CVD parameters on hydrogen permeation properties in a nano-composite SiO_2–Al_2O_3 membrane. J Membr Sci, 423–424:530–535
8. Zimmerman CM, Singh A, Koros WJ (1997) Tailoring mixed matrix composite membranes for gas separations. J Membr Sci 137:145–154
9. Aroon MA, Ismail AF, Matsuura T, Montazer-Rahmati MM (2010) Performance studies of mixed matrix membranes for gas separation: a review. Sep Purif Technol 75:229–242
10. Bhave RR (1991) Inorganic membranes synthesis, characteristics and applications. New York
11. Dun H, Zhang W, Wei Y, Xiuqing S, Li Y, Chen L (2004) Layer-by-layer self-assembly of multilayer zirconia nanoparticles on silica spheres for HPLC packings. Anal Chem 76:5016–5023
12. Campbell CT (2013) The energetics of supported metal nanoparticles: relationships to sintering rates and catalytic activity. Acc Chem Res 46(8):1712–1719
13. Coble RL, Burke JE (1963) In: Burke JE (ed) Progress in Ceramic Science. Pergamon Press, New York

14. Lin YS, Chang C-H, Gopalan R (1994) Improvement of thermal stability of porous nanostructured ceramic membranes. Ind Eng Chem Res 33:860–870
15. Chang C-H, Gopalan R, Lin YS (1994) Developmental stages of Chinese children's concepts of health and illness in Taiwan. J Membr Sci 91:27–45
16. Mercera PDL (1991) Zirconia as a support for catalysts: preparation, characterization and properties. PhD Thesis, University of Twente, The Netherlands
17. Shi JL, Lin ZX, Yen TS (1991) Effect of dopants on the crystallite growth of superfine zirconia powder. J Eur Ceram Soc 8:117–122
18. Vaßen R, Czech N, Mallener W, Stamm W, Stover D (2001) Influence of impurity content and porosity of plasma-sprayed yttria-stabilized zirconia layers on the sintering behaviour. Surf Coat Tech 141:135–140
19. Yoldas BE (1986) Zirconium oxides formed by hydrolytic condensation of alkoxides and parameters that affect their morphology. J Mater Sci 21:1080–1086
20. Rodriguez Avendano RG, De Los Reyes JA, Viveros T, Montoya De La Fuente JA (2009) Synthesis and characterization of mesoporous materials: silica–zirconia and silica–titania. Catal Today 148:12–18
21. Yoshida K, Hirano Y, Fujii H, Tsuru T, Asaeda M (2001) Hydrothermal stability and performance of silica-zirconia membranes for hydrogen separation in hydrothermal conditions. J Chem Eng Jpn, 34:523–530
22. Puthai W, Kanezashi M, Nagasawa H, Tsuru T (2017) SiO_2-ZrO_2 nanofiltration membranes of different Si/Zr molar ratios: Stability in hot water and acid/alkaline solutions. J Membr Sci 524:700–711
23. Tsuru T, Wada S-I, Izumi S, Asaeda M (1998) Silica–zirconia membranes for nanofiltration. J Membr Sci 149:127–135
24. Kelly JR, Denry I (2008) Stabilized zirconia as a structural ceramic: an overview. Dent Mater 24:289–298
25. Zakaria Z, Abu Hassan SH, Shaari N, Yahaya AZ, Kar YB (2020) A review on recent status and challenges of yttria stabilized zirconia modification to lowering the temperature of solid oxide fuel cells operation. Int J Energy Res 44:631–650
26. Tsuru T, Hino T, Yoshioka T, Asaeda M (2001) Permporometry characterization of microporous ceramic membranes. J Membr Sci 186:257–265
27. Grill A, Neumayer A (2003) Structure of low dielectric constant to extreme low dielectric constant SiCOH films: fourier transform infrared spectroscopy characterization. J Appl Phys 94(10):6697–6707
28. Wu Z-G, Zhao Y-X, Liu D-S (2004) Congenital diaphragmatic hernia: a major therapeutic challenge in pediatric critical care. Micropor Mesopor Mater 68:127–132
29. Thommes M, Kaneko K, Neimark AV, Olivier JP, Rodriguez-Reinoso F, Rouquerol J, Sing KSW (2015) Physisorption of gases, with special reference to the evaluation of surface area and pore size distribution (IUPAC Technical Report. Pure Appl Chem 87 (9–10):1051–1069
30. Sotomayor F, Cychosz KA, Thommes M (2018) Characterization of micro/mesoporous materials by physisorption: concepts and case studies. Acc Mater Surf Res 3(2):34–50
31. Torres-Rodrígueza J, Kalmár J, Menelaou M, Čelko L, Dvořak K, Cihlář J, Cihlař Jr J, Kaiser J, Győri E, Veres P, Fábián I, Lázár I (2019) Heat treatment induced phase transformations in zirconia and yttria-stabilized zirconia monolithic aerogels. J Supercrit Fluid 149:54–63
32. Moulder JF, Stickle WF, Sobol PE, Bomben KD (1992) Handbook of X-ray Photoelectron Spectroscopy. pp. 106-107 Perkin Elmer, Minnesota
33. Hassan NS, Jalil AA, Triwahyono S, Hitam CNC, Rahman AFA, Khusnun NF, Mamat CR, Asmadi M, Mohamed M, Ali MW, Prasetyoko D (2018) Exploiting copper–silica–zirconia cooperative interactions for the stabilization of tetragonal zirconia catalysts and enhancement of the visible-light photodegradation of bisphenol A. J Taiwan Inst Chem E 82:322–330
34. Liu W, Zhang B, Liu X, Xu L (2006) Thermal stability of silica-zirconia membranes. Chinese J Chem Eng 14(1):30–36
35. Hishita S, Mutoh I, Koumoto K, Yanagida H (1983) Inhibition mechanism of the anatase-rutile phase transformation by rare earth oxides. Ceram Int 9(2):61–67
36. Bosman HJM, Pijpers AP, Jaspers AW (1996) An X-Ray photoelectron spectroscopy study of the acidity of SiO_2–ZrO_2 mixed oxides Catal 161:551–559
37. Majumdar D, Chatterjee D (1991) X-ray photoelectron spectroscopic studies on yttria, zirconia, and yttria-stabilized zirconia. J Appl Phys 70(2):988–992
38. Pyen S, Hong E, Shin M, Suh Y-M, Shin C-H (2018) Acidity of co-precipitated SiO_2-ZrO_2 mixed oxides in the acid-catalyzed dehydrations of iso-propanol and formic acid. Mol Catal 448:71–77
39. Damyanova S, Grange P, Delmon B (1997) Surface characterization of zirconia-coated alumina and silica carriers Catal 168:421–430
40. Xia W, Wang Y, Hagen V, Heel A, Kasper G, Patil U, Devi A, Muhler M (2007) The synthesis of ZrO_2/SiO_2 nanocomposites by the two-step CVD of a volatile halogen-free Zr alkoxide in a fluidized-bed reactor. Chem Vap Depos 13:37–41
41. Tsunekawa S, Asami K, Ito S, Yashima M, Sugimoto T (2005) XPS study of the phase transition in pure zirconium oxide nanocrystallites. Appl Surf Sci 252:1651–1656
42. Matsui K (2007) Sintering kinetics at isothermal shrinkage: II, effect of Y_2O_3 concentration on the initial sintering stage of fine zirconia powder. J Am Ceram Soc 90(2):443–447